Available online at www.sciencedirect.com

ScienceDirect

Ceramics International 40 (2014) 4025–4031

CERAMICS INTERNATIONAL

www.elsevier.com/locate/ceramint

Effects of aluminium doping on structural and photoluminescence properties of ZnO nanoparticles

Gunjan Srinet, Ravindra Kumar*, Vivek Sajal

Department of Physics and Materials Science and Engineering, Jaypee Institute of Information Technology, Noida-201307, Uttar Pradesh, India

Received 17 June 2013; received in revised form 10 August 2013; accepted 10 August 2013
Available online 16 August 2013

Abstract

Structural and optical properties of Al doped ZnO nanoparticles prepared by the thermal decomposition method are presented. X-ray diffraction studies confirmed the substitution of Al on Zn sites without changing the hexagonal structure of ZnO. Also, lattice parameters, the crystallite size and other physical parameters such as strain, stress and energy density were calculated from various modified forms of W–H equation and their variation with the doping of Al is discussed. A blue shift in the energy band gap attributed to increase in carrier concentration (Burstein Moss Effect) is observed by absorption spectra. Photoluminescence studies show a strong and dominant peak corresponding to the near band edge emission in ultraviolet range and a broad band in the range 420–520 nm corresponding to defects and oxygen vacancies. Phonon modes were studied by FTIR measurements. The tunability of the band gap of ZnO nanoparticles could eventually be useful for potential optoelectronic applications.

Keywords: C. Optical properties; D. ZnO; Photoluminescence studies

1. Introduction

Zinc oxide has attracted the scientific community because of its versatile applications in short wavelength light emitting diodes and lasers owing to its wide direct band gap (3.37 eV) at room temperature, large exciton binding energy (60 meV), excellent chemical and thermal stability and low cost [1,2]. Several recent studies have examined for the fabrication and properties of ZnO thin films having potential applications in solar cells, gas sensors, piezoelectric transducers, varistors and photocatalysts with high chemical activity [3,4].

Due to the quantum confinement, doped ZnO nanoparticles exhibit unique and novel properties as compared to bulk counterparts [3]. Nevertheless, properties of doped ZnO nanoparticles are closely associated with structural parameters. In the past few years, several groups have studied doped ZnO systems for various properties having potential applications in spintronics and optoelectronic devices [5–12]. It was observed that Al is one of the most efficient materials for enhancement of optical and electrical properties of ZnO. Kadam et al. [10] studied the grain size related optical band gap changes in ZnO nanocrystals synthesised by wet chemical route, Lo et al. [11] presented a detailed Raman scattering and studied band gap variations with lattice defects of Al doped ZnO nanoparticles synthesised by chemical colloid process and Godani et al. [12] studied the structure dependent optical and electrical properties of Al doped ZnO nanostructures. Moreover, the particle size and shape can be controlled by using suitable precursor solution with appropriate surfactant. There is no significant reports available in the literature on the detailed structural analysis of Al doped ZnO nanoparticles up to high level of doping concentration. Under this scenario, we prepared diethanolamine (DEA) assisted Al doped ZnO nanoparticles by thermal decomposition method and carefully studied the role of Al doping on the structural, vibrational and optical properties.

2. Experimental details

Al doped ZnO nanopowders were synthesised by the thermal decomposition method by using chemicals of analytical grade. Initially, 0.16 mol $C_2H_5O_4 \cdot 2H_2O$ (oxalic acid) was dissolved in 100 ml of deionised (DI) water with vigorous

*Corresponding author. Tel.: +91 9999762428.
E-mail address: ravindrakbhatt@gmail.com (R. Kumar).

0272-8842/$ - see front matter © 2013 Elsevier Ltd and Techna Group S.r.l. All rights reserved.
http://dx.doi.org/10.1016/j.ceramint.2013.08.055

stirring. Then, 0.02 mol DEA is added to get homogenous DEA/$C_2H_5O_4 \cdot 2H_2O$ (A) solution. Now, 0.02 mol zinc acetate dihydrate ($Zn(CH_3COO)_2 \cdot 2H_2O$) was dissolved in 100 ml of DI water. The appropriate amount of aluminium chloride hexahydrate ($AlCl_3 \cdot 6H_2O$) was added to get the solution B. Finally, B was added dropwise in the aqueous A solution. White precipitates were formed and the suspension was continuously stirred at room temperature and put for 12 h to settle down. Then, precipitates were filtered, washed with DI water and ethanol water several times, dried at room temperature and calcined at 600 °C for 1 h.

The crystalline structure and the phase purity of samples were confirmed by X-ray diffraction (XRD) measurements (Shimadzu XRD-6000 with CuKα ($\lambda = 1.5406$ Å) radiation). Fourier transform infrared spectroscopy (FTIR) measurements were done by using a Perkin Elmer BX-IV spectrophotometer through KBr pellet technique in the range 400–4000 cm^{-1}. Absorption spectra were carried out by a Perkin Elmer Lambda-35 UV–visible spectrometer in the wave-length range 300–800 nm. Photoluminescence (PL) spectra of samples were acquired using xenon flash lamp laser as excitation source by a Perkin Elmer Lambda luminescence spectrophotometer (LS-55).

3. Results and discussion

3.1. Structural analysis

Fig. 1(a) shows the XRD pattern of $Zn_{1-x}Al_xO$ ($x = 0.02$, 0.04, 0.06, 0.08 and 0.1) nanoparticles for various doping levels in which diffraction peaks are indexed to the wurtzite structure of ZnO (space group P63mc). There is no indication of any secondary phases or clusters, confirming the single phase of samples. It also confirms that dopants have not altered the basic wurtzite crystal structure of samples.

Diffraction peak positions of XRD signals show a slight shift towards higher angles up to the doping levels $x = 0.10$. The shift towards the higher angles may be due to the shrinkage caused by the substitution of Al^{3+} (radius 0.53 Å) on Zn^{2+} sites (0.60 Å) [13]. Furthermore, the observed broadening of peaks may be due to the formation of smaller grains as a result of an increase in disorder by aluminium doping as shown in Fig. 1(b). Variation of lattice parameters 'a' and 'c' and the unit cell volume decreases with Al doping concentration is shown in Fig. 1(c) and (d).

XRD can also be utilised to evaluate the peak broadening with crystallite size and the lattice strain due to dislocations [14]. The average crystallite size of Al doped ZnO nanoparticles was determined by the broadening in the XRD pattern by using the Scherrer formula: $d_{hkl} = k\lambda/(\beta_{hkl} \cos\theta_{hkl})$, where d_{hkl} is the crystallite size, k is the shape factor (0.9), β_{hkl} is the full width of half maxima of the instrumental corrected broadening, λ is the wavelength of radiation (1.5403 Å) and θ_{hkl} is the peak position. Calculated average crystallite sizes are concluded in Table 1.

The instrumental corrected broadening (β_{hkl}) is corrected for each peak of Al doped ZnO nanostructure by using the relation:

$$\beta_{hkl} = \sqrt{(\beta_{hkl})^2_{measured} - (\beta_{hkl})^2_{instrumental}}$$

The strain induced broadening in nanoparticles due to crystal imperfections and distortions is given by $\beta_{hkl} = 4\varepsilon \tan\theta_{hkl}$, where '$\varepsilon$' is the microstrain.

Williamson [15] proposed the dependency of the diffraction line broadening on the crystallite size and strain contribution as: $\beta_{hkl} = (K\lambda/d_{hkl} \cos\theta_{hkl}) + (4\varepsilon \tan\theta_{hkl})$. This may be further simplified to $\beta_{hkl} \cos\theta_{hkl} = (K\lambda/d_{hkl}) + (4\varepsilon \sin\theta_{hkl})$, which is called Williamson Hall (W–H) equation. Now, $\beta_{hkl} \cos\theta_{hkl}$ is plotted as a function of 4 $\sin\theta_{hkl}$ (as shown in Fig. 2(a)) as a straight line and the slope is calculated which is microstrain ε and y-intercept of the fit gives the crystallite size. This method was applied to all samples and calculated microstrains and crystallite sizes are shown in Table 1. A clear increase in the strain is observed with increase in Al doping concentration (Fig. 2(d)), which may be due to lattice mismatch with increase in the concentration [15]. The above model of strain calculation is called uniform deformation model (UDM), in which the strain is assumed to be uniform in all crystallographic directions. But, as material properties are anisotropic; so, the assumption of UDM is no longer valid.

In uniform stress deformation model (USDM), uniform stress deformation (σ) is expressed in terms of the strain (ε) as $\sigma = E_{hkl}\varepsilon_{hkl}$, where E_{hkl} is young's modulus in the direction perpendicular to the plane, which has the form

$$E_{hkl} = \frac{[h^2 + ((h+2k)^2/3) + (al/c)^2]}{S_{11}(h^2 + (h+2k)^2/3) + S_{33}(al/c)^4 + (4S_{13} + S_{44})(h^2(h+2k)^2/3)(al/c)^2}$$

for the present hexagonal crystals [16], where a and c are lattice parameters and S_{11}, S_{22}, S_{33} and S_{44} are elastic compliances of ZnO and their values are 7.858×10^{-12}, -2.206×10^{-12}, 6.940×10^{-12} and 23.57×10^{-12}, respectively [17,18]. Now, the W–H equation will be of the form $\beta_{hkl} \cos\theta_{hkl} = (K\lambda/d_{hkl}) + (4\sigma \sin\theta_{hkl}/E_{hkl})$ [19]. Now, $\beta_{hkl} \cos\theta_{hkl}$ is plotted against 4 $\sin\theta_{hkl}/E_{hkl}$ for all samples (Fig. 2(b)). Slopes of linear fits are the stress (σ) and intercepts of fitted lines give the crystallite size (d_{hkl}). Calculated values of crystallite size and stress are shown in Table 1. An increase in the stress is obtained with increase in Al concentration (Fig. 2(d)).

For an elastic system that follows Hooke's law, the young modulus E_{hkl} and strain ε_{hkl} are connected to the deformation energy density 'u' by the relation $u = \varepsilon^2 E_{hkl}/2$ [13]. So, the modified W–H equation can be written in the form of energy and strain as: $\beta_{hkl} \cos\theta_{hkl} = (k\lambda/D) + (4 \sin\theta_{hkl}(2u/E_{hkl})^{1/2})$. The uniform deformation energy density can be calculated from the slope of the fitted line between the $\beta_{hkl} \cos\theta_{hkl}$ and $2^{5/2} \sin\theta_{hkl} E_{hkl}^{-1/2}$ and the crystallite size d_{hkl} from the y-intercept as shown in Fig. 2(c). This model is called uniform deformation energy density model (UDEDM). Variations of stress and deformation energy density with the Al concentration are shown in Fig. 2(d). Also, we can see from Table 1 that the crystallite sizes calculated from various models are approximately same.

3.2. Optical properties

Optical absorbance spectra were recorded by dispersing the nanopowder in spectroscopic grade ethanol, which was also

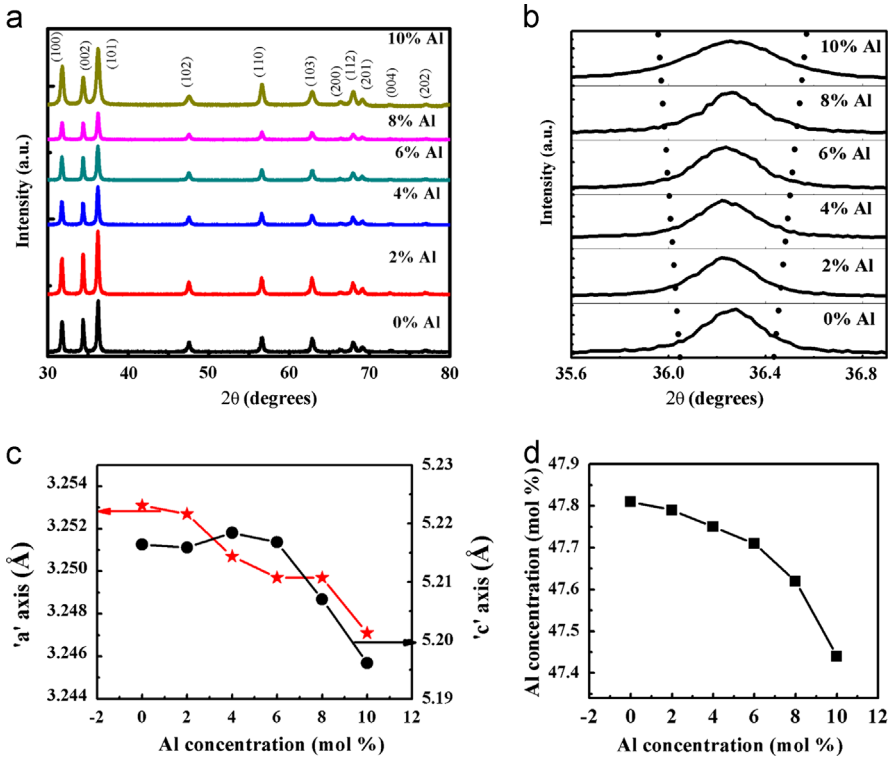

Fig. 1. (a) X-ray diffraction patterns of the prepared nanoparticles. (b) Doping-induced peak shift. (c) Variation of lattice parameter '*a*' and '*c*' with Al concentration. (d) Variation of unit cell volume with Al concentration.

Table 1
Geometric parameters of $Zn_{1-x}Al_xO$ nanoparticles by Williamson–Hall analysis.

Al concentration *x*	Crystallite size (nm) by Scherrer formula	Williamson–Hall analysis					
		UDM		USDM		UDEDM	
		Crystallite size (nm)	Strain × 10^{-4}	Crystallite size (nm)	Stress (MPa)	Crystallite size (nm)	Energy density (J m^{-3})
0	39	30	3.2	29	38	30	6414
0.02	37	29	1.3	29	15.63	29	1069
0.04	36	28	1.9	28	21.85	28	2199
0.06	34	28	3.4	27	39.3	28	6822
0.08	32	27	3.6	27	40.45	27	7225
0.1	31	26	3.8	26	41.09	27	7903

used as reference. Optical absorbance spectra of pure and Al doped ZnO nanoparticles are shown in Fig. 3(a). It can be clearly observed that the absorption edge shifted towards the lower wavelength with increase in the Al concentration.

According to the theory of the optical absorption, the absorption coefficient α and the photon energy $h\nu$ for direct allowed transitions are related as: $(\alpha h\nu)^2 = A(h\nu - E_g)$, where the constant A is a constant function. The direct energy gap is determined by extrapolating the straight line portion of the $(\alpha h\nu)^2$ versus $h\nu$ plot (Tauc plot) to intersect the energy axis at $\alpha = 0$ (Fig. 3(b)).

The energy band gap of nanoparticles shows the clear dependence of Al doping concentration. The effect of Al concentration on the absorption edge of ZnO nanoparticles results in a blue shift in the cut-off wavelength and this observed shift is proportional to the amount of Al present in the sample (Fig. 3(c)). The optical band gap of the samples has been calculated and found to increase in band gap with Al concentration is observed up to 10% Al doping. The blue shift behaviour in the band gap can be attributed to an increase in the carrier concentration that blocks the lowest states in the conduction band, known as the Burstein–Moss effect [20], which is frequently observed in naturally n-type semiconductors. An increase in the carrier concentration in Al doped ZnO will cause the Fermi level to move into the conduction band.

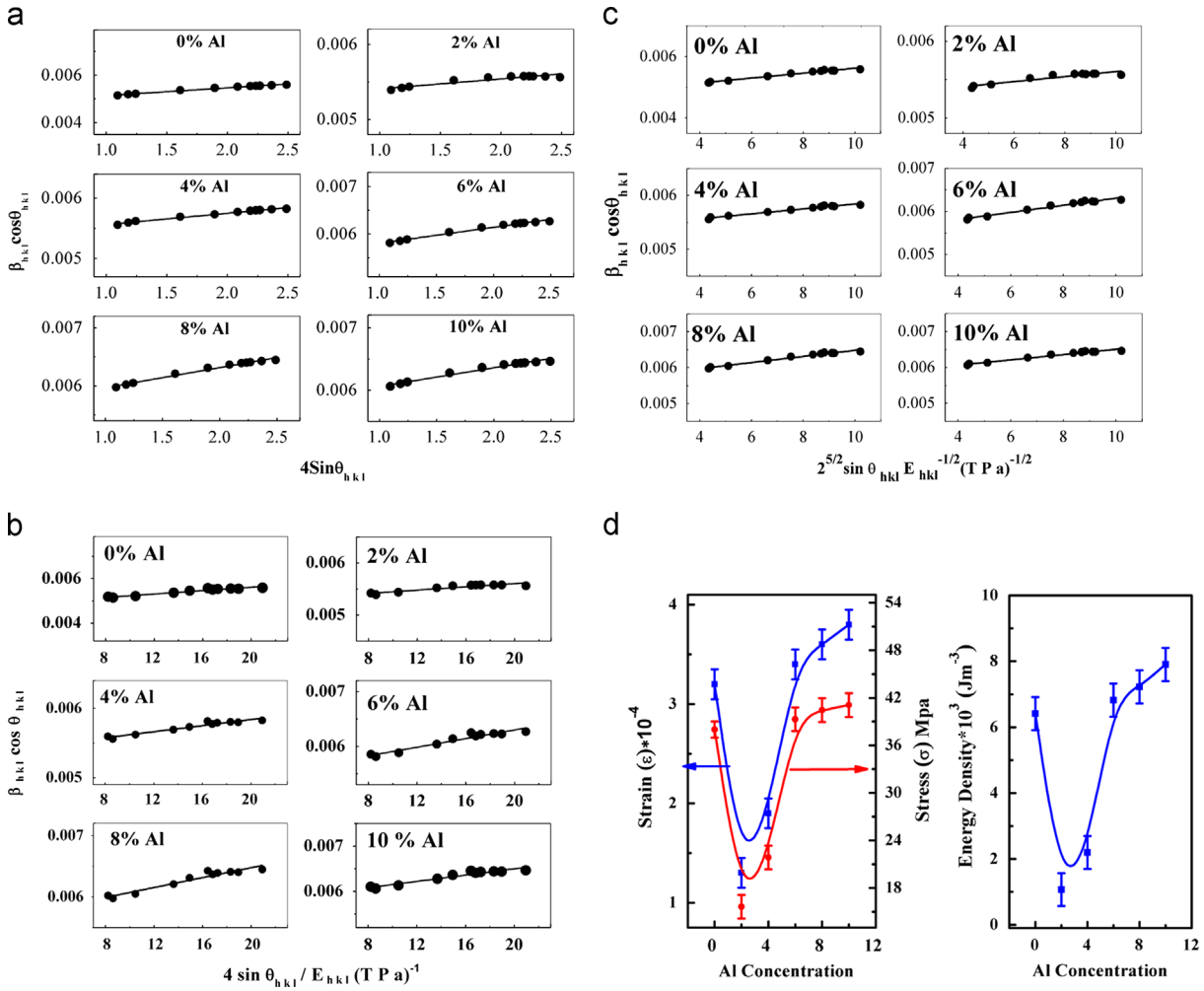

Fig. 2. (a) The W–H analysis assuming UDM. (b) The modified form of W–H analysis assuming USDM. (c) The modified form of W–H analysis assuming UDEDM. (d) Variation of calculated parameters with Al concentration.

Thus, the low energy transitions are blocked [21,22]. The filling of the conduction band by electrons generally causes a blue shift in the band gap.

Room temperature PL spectra of Al doped ZnO samples are shown in Fig. 4, which were taken by using an excitation wavelength of 325 nm. Typically, two bands have appeared in the spectra, the near band edge (NBE) emission a in the UV region (A) originated due to the recombination of free excitons and broad deep level emission in the visible region caused by impurities and structural defects of crystals [23]. A blue shift in NBE emission (around 375 nm) in emission spectra is observed which is similar to the blue shift in the band edge in the absorption spectra.

The inset (a) of Fig. 4 shows the broad emission band corresponding to defect states. It can be clearly seen that the intensity of defect states continuously increases with Al concentration which can be understood by considering the Al incorporation process in nanoparticles. The Al^{3+} ions can incorporate into the ZnO nanostructures in two different ways creating oxygen vacancies or incorporating as interstitials, while at low doping concentration (2%), most of the Al^{3+} ions are substituted. For the higher doping concentration, the excess Al^{3+} ZnO nanoparticles incorporate interstitially, creating large amount of lattice defects.

The broad visible emission band could be deconvoluted into Gaussian shaped components shown in the inset (b) of Fig. 4, which corresponds to the blue and green emission. The blue emission peaks are at around 452 and 480 nm assigned to the energy of transition of electron from interstitial Zn (Zn_i) to Zn vacancies (V_{Zn}) [24] and to the transition between the oxygen vacancy and interstitial oxygen (O_i) respectively [24]. The green emission peak around 505 nm could be due to the transition from Zn_i levels to O_i. The emission around 529 nm is debatable and may be due to several types of defects such as V_O (oxygen vacancies), Zn_i, V_{Zn} and O_i [25,26]. On the other hand component bands appeared at about 580 and 640 nm are frequently assigned as yellow and orange emissions in ZnO, respectively, and associated with the excess oxygen and Zn_i [27]. It can be clearly seen in Fig. 4 that the intensity of yellow emission clearly increases with doping concentration and shows the sharp peak for 10% Al doped ZnO nanoparticles. The intensity of near band edge UV emission is highest, accompanied

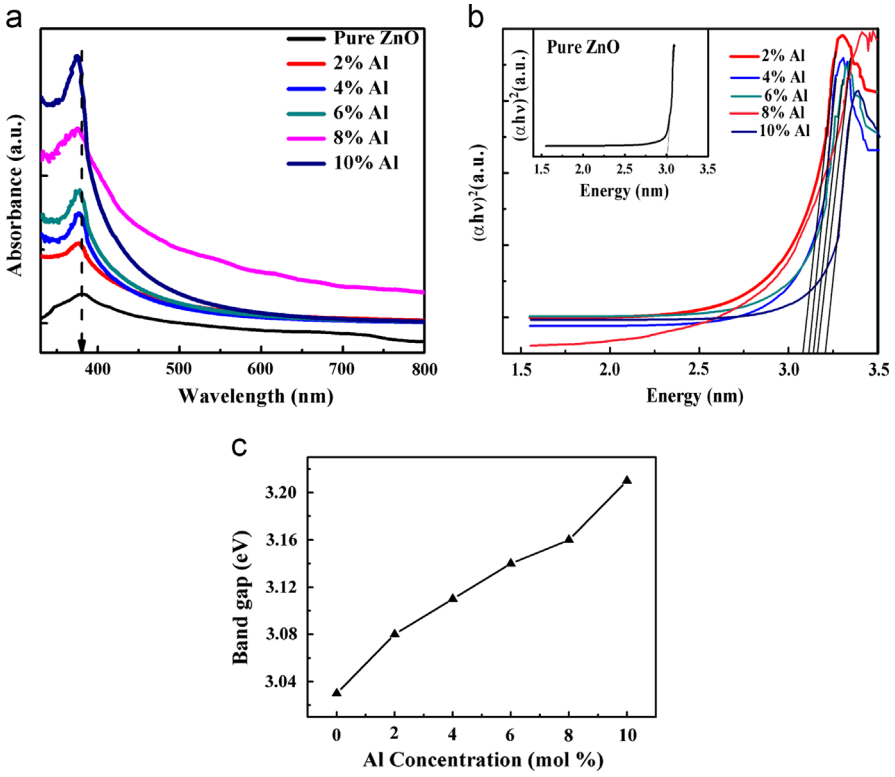

Fig. 3. (a) UV–vis spectra of the Al-doped ZnO nanoparticles. (b) Plot of the absorption coefficient versus photon energy. (c) Variation of the band gap with Al concentration.

by broad visible emission bands. Thus, we conclude that the Al-doping leads to a blue shift in NBE and increase in the intrinsic defects such as V_O and O_{Zn} density [28].

3.3. Phonon properties

FTIR measurements were performed in the range 400–4000 cm^{-1} and are displayed in Fig. 5. Absorption peaks observed around 2365 cm^{-1} are assigned to the CO_2 mode, which may be due to the atmospheric CO_2 in the atmosphere [23]. Two absorption peaks at 1560 and 1435 cm^{-1} are corresponding to the asymmetric ν_{as} (COO^-) and symmetric stretching ν_s (COO^-) vibrations of acetate species [29]. The band at 1635 cm^{-1} has been allotted to the first overtone of the crucial stretching mode of OH which indicates the presence of bound H_2O on the surface of the sample [30]. The IR active characteristic broad band (optical phonon modes) of ZnO is observed in the spectral range 400–600 cm^{-1}. Absorption bands are found to blue shift up to 8% of Al and red shift for 10% Al doped ZnO nanoparticles.

The observed change in the peak positions of the ZnO absorption bands reflects that the Zn–O–Zn network is perturbed by the presence of Al in its environment. For the exact positions of the Zn–O bands, IR band in the region 400–600 cm^{-1} is shown in Fig. 6(a). These bands are fitted by Gaussian and show the three bands A_1, A_2 and A_3 (inset of Fig. 6(a)). According to the previous literature [20,31], the band A_1 around 435 cm^{-1} corresponds to the E_1(TO) mode. Bands centred at 493 cm^{-1} (A_2) and 540 cm^{-1} (A_3) are

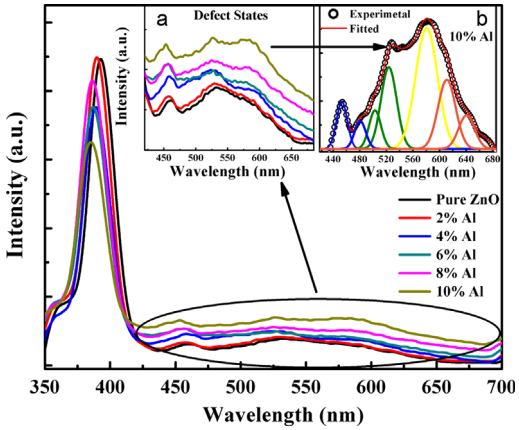

Fig. 4. PL spectra of $Zn_{1-x}Al_xO$ nanoparticles. Inset :(a) variation of defect states with doping and (b) defect state of 10% Al doped ZnO nanoparticles fitted with Gaussian.

surface phonon modes (SPM) and named as SPM [A_1(TO)] and SPM [E_1(TO)], respectively, which normally appear when the prepared particles are smaller than the incident IR wavelength [31]. The IR bands correspond to Zn showing a variation in the vibrational frequencies with increase in the doping concentration of Al, as shown in Fig. 6(b). The shift in the band position on doping of Al may be due to the difference in ionic radii of Zn and Al as well the structural changes induced due to the doping [32]. The average bond length of Zn(Al)–O in $Zn_{1-x}Al_xO$ can be determined from the band position of E_1(TO) and by the relation $\nu = (1/2\pi c)(k/\mu)^{1/2}$,

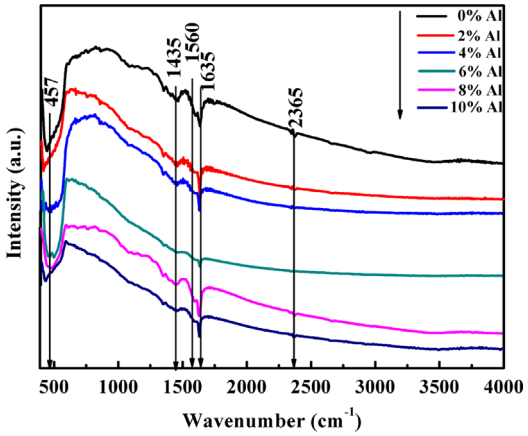

Fig. 5. The FTIR full scan transmittance spectra of $Zn_{1-x}Al_xO$ nanoparticles.

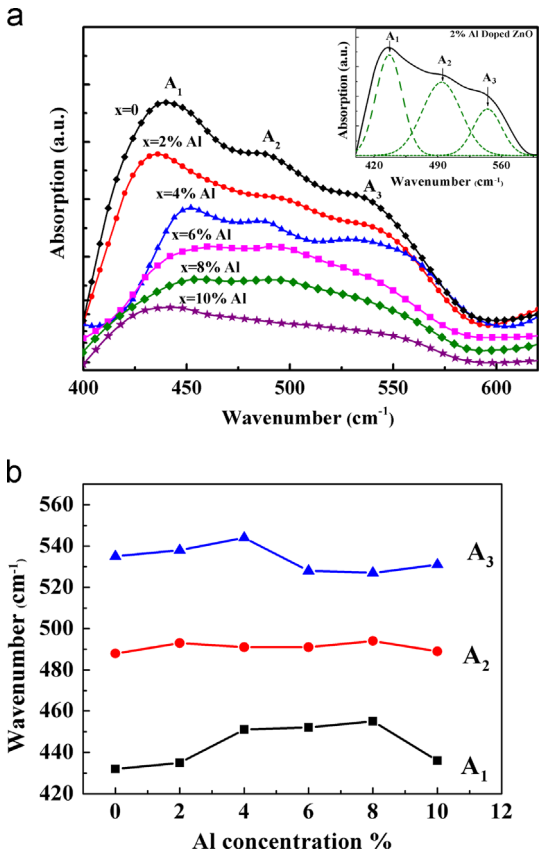

Fig. 6. (a) FTIR spectra corresponding to Zn–O bonds (inset shows Zn–O bonds with gaussian fitting for a typical sample). (b) Variation of peak wavenumber with Al concentration.

where ν is the wavenumber, c is the velocity of light, k is the average force constant of the Zn(Al)–O bond and μ is the effective mass of the bond which is given by the relation:

$$\mu = \frac{M_O[xM_{Al}+(1-x)M_{Zn}]}{M_O+[xM_{Al}+(1-x)M_{Zn}]},$$

where M_O, M_{Zn} and M_{Al} are the atomic weights of the O, Zn and Al, respectively and force constant is related to the average Zn(Al)–O bond length (Å) by the equation $k = 17/r^3$ [33].

Table 2
The IR band and local structure data of Zn(Al)–O bonds of $Zn_{1-x}Al_xO$ nanoparticles.

Samples ($Zn_{1-x}Al_xO$)	Wavenumber (cm^{-1})	Effective mass (atomic weight)	Force constant ($N\,m^{-1}$)	Bond length (Å)
$x=0$	432	12.608	134.49	2.3068
$x=0.02$	435	12.8179	143.0769	2.2819
$x=0.04$	451	12.7874	153.40	2.2295
$x=0.06$	452	12.7548	153.69	2.2280
$x=0.08$	455	12.7245	155.37	2.2175
$x=0.10$	436	12.6922	142.35	2.286

Calculated values of effective mass, force constant and bond length are listed in Table 2.

It can be observed that the effective mass of Zn (Al)–O bond decreased with Al substitution because of lower atomic weight of Al than that of Zn. Also the average force constant decreased with Al substitution which results an increment in the average Zn (Al)–O bond length.

4. Conclusions

In summary, phase pure Al doped ZnO nanoparticles were successfully prepared by the DEA assisted thermal decomposition method. The substitution of Zn sites by Al^{3+} ions in wurtzite ZnO was confirmed by XRD. The line broadening due to small crystallite size and strain was analysed by various modified forms of W–H equation. It was observed that the strain, stress and energy density increased with Al doping. FTIR spectroscopic measurements show a broad band in the range 600–400 cm^{-1}, composed of three distinct peaks assigned to E_1(TO), SPM A_1(TO) and SPM E_1(TO) modes. The calculated effective mass of Zn (Al)–O bond decreased with Al substitution because of lower atomic weight of Al than that of Zn. Also, the average force constant decreased with Al substitution which results in an increment in the average Zn (Al)–O bond length. The energy band gap of samples shows the variation from 3.03 to 3.21 eV; increase in the band gap is attributed to the Burstein–Moss shift caused by the Al doping of the ZnO. Room temperature PL measurements illustrate strong NBE emissions, followed by a broad band in the range 450–650 nm attributed to defects and vacancies. The tunability of optical properties of ZnO nanoparticles by Al doping could be useful for potential optoelectronic applications.

References

[1] U. Ozgur, Ya.I. Alivov, C. Liu, A. Teke, M.A. Reshchikov, S. Dogan, V. Avrutin, S.J. Cho, H. Morkoc, A comprehensive review of ZnO materials and devices, Journal of Applied Physics 98 (2005) 041301.
[2] A.A. Baladin, K.L. Wang, Handbook of Semiconductor Nanostructures and Nanodevices, American Scientific Publisher, Los Angeles, 2006.
[3] C. Klingshirn, J. Fallert, H. Zhou, J. Sartor, C. Thiele, F. Maier-Flaig, D. Schneider, H. Kalt, 65 years of ZnO research—old and very recent results, Physica Status Solidi B247 (2010) 1424.
[4] M.D. McCluskey, S.J. Jokela, Defects in ZnO, Journal of Applied Physics 106 (2009) 071101.

[5] P. Banerjee, W.J. Lee, K.R. Bae, S.B. Lee, G.W. Rubloff, Structural, electrical, and optical properties of atomic layer deposition Al doped ZnO films, Journal of Applied Physics 108 (2010) 04350410.
[6] X.L. Wang, Q. Shao, C.W. Leung, A. Ruotolo, Non-volatile, reversible switching of the magnetic moment in Mn-doped ZnO films, Journal of Applied Physics 113 (2013) 17C301.
[7] R.E. Treharne, K. Hutchings, D.A. Lamb, S.J.C. Irvine, D. Lane, K. Durose, Combinatorial optimization of Al-doped ZnO films for thin-film photovoltaics, Journal of Physics D: Applied Physics 45 (2012) 335102.
[8] J. Han, F. Fan, C. Xu, S. Lin, M. Wei, X. Duan, Z.L. Wang, ZnO nanotube-based dye-sensitized solar cell and its application in self-powered devices, Nanotechnology 21 (2010) 405203.
[9] H. Gu, W. Zhang, Y. Xu, M. Yan, Effect of oxygen deficiency on room temperature ferromagnetism in Co doped ZnO, Applied Physics Letter 100 (2012) 202401.
[10] P. Kadam, C. Agashe, S. Mahamuni, Al doped ZnO nanocrystals, Journal of Applied Physics 104 (2008) 103501.
[11] S.-S. Lo, D. Huang, C.H. Tu, C.-H. Hou, C.-C. Chen, Raman scattering and band-gap variations of Al-doped ZnO nanoparticles synthesised by a chemical colloid process, Journal of Physics D: Applied Physics 42 (2009) 095420.
[12] P. Gondoni, M. Ghidelli, F. Di Fonzo, M. Carminati, V. Russo, A. Li Bassi, C.S. Casari, Structure-dependent optical and electrical transport properties of nanostructured Al-doped ZnO, Nanotechnology 23 (2012) 365706.
[13] S.C. Navale, V. Ravi, S. Mulla, S.W. Gosavi, S.K. Kulkarni, Low temperature synthesis and NO_x sensing properties of nanostructured Al-doped ZnO, Sensors and Actuators B 126 (2007) 382.
[14] R. Yogamalar, R. Srinivasan, A. Vinu, K. Ariga, A.C. Bose, X-ray peak broadening analysis in ZnO nanoparticles, Solid State Communications 149 (2009) 1919.
[15] R. Bhargava, P.K. Sharma, S. Kumar, A.C. Pandey, N. Kumar, Consequence of doping mediated strain and the activation energy on the structural and optical properties of ZnO:Cr nanoparticles, Journal of Solid State Chemistry 183 (2010) 1400.
[16] J.M. Zhang, V. Zhanga, K.W. Xub, V. Jic, General compliance transformation relation and applications for anisotropic hexagonal metals, Solid State Communications 139 (2006) 87.
[17] J.F. Nye, Physical Properties of Crystals: Their Representation by Tensors and Matrices, Oxford, New York, 1985.
[18] T. Pandiyarajan, B. Karthikeyan, Cr doping induced structural, phonon and excitonic properties of ZnO nanoparticles, Journal of Nanoparticle Research 14 (2012) 647.
[19] Y. Rosenberg, V.S. Machavariani, V. Voronel, S. Garber, A. Rubshtein, A.I. Frenkel, E.A. Stern, Strain energy density in the x-ray powder diffraction from mixed crystals and alloys, Journal of Physics: Condensed Matter 12 (2000) 8081.
[20] E. Burstein, Anomalous optical absorption limit in InSb, Physical Review 93 (1954) 632.
[21] T.S. Moss, The interpretation of the properties of indium antimonide, Proceedings of the Physical Society, London, Section B 67 (1954) 775.
[22] K. Sakai, T. Kakeno, T. Ikari, S. Shirakata, T. Sakemi, K. Awai, T. Yamamoto, Defect centers and optical absorption edge of degenerated semiconductor ZnO thin films grown by a reactive plasma deposition by means of piezoelectric photothermal spectroscopy, Journal of Applied Physics 99 (2006) 043508.
[23] Y.-M. Hao, S.-Y. Lou, S.-M. Zhau, R.-J. Yuan, G.-Y. Zhu, N. Li, Structural, optical, and magnetic studies of manganese-doped zinc oxide hierarchical microspheres by self-assembly of nanoparticles, Nanoscale Research Letters 7 (2012) 100.
[24] P.S. Xu, Y.M. Sun, C.S. Shi, F.Q. Xu, H.B. Pan, The electronic structure and spectral properties of ZnO and its defects, Nuclear Instruments and Methods in Physics Research Section B 199 (2003) 286.
[25] S. Mahamuni, K. Borgohain, B.S. Bendre, V.J. Leppert, S.H. Risbud, Spectroscopic and structural characterization of electrochemically grown ZnO quantum dots, Journal of Applied Physics 85 (1999) 2861.
[26] G. Srinet, P. Varshneya, R. Kumar, V. Sajal, P.K. Kulriya, M. Knobel, S. K. Sharma, Structural, optical and magnetic properties of $Zn_{1-x}Co_xO$ prepared by the sol–gel route, Ceramics International 39 (2013) 6077–6085.
[27] R.S. Zeferino, M.B. Flores, U. Pal, Photoluminescence and Raman scattering in Ag-doped ZnO nanoparticles, Journal of Applied Physics 109 (2011) 014308.
[28] N.S. Sabri, A.K. Yahya, M. Kumar Talari, Emission properties of Mn doped ZnO nanoparticles prepared by mechanochemical processing, Journal of Luminescence 132 (2012) 1735.
[29] G. Srinet, R. Kumar, V. Sajal, Effects of Ni doping on structural, optical and dielectric properties of ZnO, Ceramics International 39 (2013) 7557.
[30] J. Singh, P. Kumar, K.S. Hui, K.N. Hui, K. Ramam, R.S. Tiwari, O. N. Srivastava, Synthesis, band-gap tuning, structural and optical investigations of Mg doped ZnO nanowires, CrystEngComm 14 (2012) 5898.
[31] C. Bundesmann, M. Schubert, D. Spemann, T. Butz, M. Lorenz, E.M. Kaidashev, M. Grundmann, N. Ashkenov, H. Neumann, G. Wagner, Infrared dielectric functions and phonon modes of wurtzite $Mg_xZn_{1-x}O$ ($x \leq 0.2$), Applied Physics Letter 81 (2002) 2376.
[32] M. Ghosh, N. Dilawar, A. Bandyopadhyay, A. Raychaudhuri, Phonon dynamics of Zn(Mg,Cd)O alloy nanostructures and their phase segregation, Journal of Applied Physics 106 (2009) 084306.
[33] R. El-Mallawany, Theroretical and experimental IR spectra of binary rare earth tellurite glasses, Infrared Physics 781 (1989) 29.